Observations of Backscatter from Sand and Gravel Seafloors Between 170-250 kHz

Thomas C. Weber
University of New Hampshire - Main Campus, thomas.weber@unh.edu

Larry G. Ward
University of New Hampshire, lgward@ad.unh.edu

Recommended Citation

T. C. Weber and L. G. Ward, 'Observations of backscatter from sand and gravel seafloors between 170 and 250 kHz', The Journal of the Acoustical Society of America, vol. 138, no. 4, pp. 2169–2180, Oct. 2015.

Observations of backscatter from sand and gravel seafloors between 170 and 250 kHz

Thomas C. Weber[a]

Center for Coastal and Ocean Mapping and Department of Mechanical Engineering, University of New Hampshire, 24 Colovos Road, Durham, New Hampshire 03824, USA

Larry G. Ward

Center for Coastal and Ocean Mapping and Department of Earth Sciences, University of New Hampshire, 24 Colovos Road, Durham, New Hampshire 03824, USA

Interpreting observations of frequency-dependence in backscatter from the seafloor offers many challenges, either because multiple frequencies are used for different observations that will later be merged or simply because seafloor scattering models are not well-understood above 100 kHz. Hindering the understanding of these observations is the paucity of reported, calibrated acoustic measurements above 100 kHz. This manuscript seeks to help elucidate the linkages between seafloor properties and frequency-dependent seafloor backscatter by describing observations of backscatter collected from sand, gravel, and bedrock seafloors at frequencies between 170 and 250 kHz and at a grazing angle of 45°. Overall, the frequency dependence appeared weak for all seafloor types, with a slight increase in seafloor scattering strength with increasing frequency for an area with unimodal, very poorly to moderately well sorted, slightly granular to granular medium sand with significant amounts of shell debris and a slight decrease in all other locations.
© 2015 Acoustical Society of America. [http://dx.doi.org/10.1121/1.4930185]

I. INTRODUCTION

Observations of acoustic backscatter from the seafloor are of great interest to geologists, benthic ecologists, ecosystem managers, and other scientists who wish to discriminate between seafloor types (e.g., mud, sand, and gravel). Many of these observations are collected with multibeam echosounders (MBESs) (Lurton, 2010) which typically operate at frequencies of 100 kHz and above in near-coastal waters (i.e., less than a few hundred meters water depth) and collect data over a wide range of seabed incidence angles. End-users of MBES seafloor backscatter data are often interested in either generating mosaics of seafloor backscatter, where the inherent angle-dependence in the seafloor backscatter has been heuristically removed and "adjusted" to some oblique incidence angle (e.g., 45°) (e.g., Rzhanov et al., 2012); or inverting the angle-dependent measurements of backscatter to determine seafloor properties such as grain size (e.g., Fonseca and Mayer, 2007). Both uses of seafloor backscatter offer challenges in interpretation. For example, seafloor backscatter mosaics are sometimes generated by different MBES systems in scenarios where a change in observed acoustic backscatter can be due to either a change in seafloor type or a change in operating frequency, confounding the discrimination between different types of seafloors. In addition, inversions of angle-dependent backscatter rely at least in part on interface scattering models that are not well-understood at frequencies above 100 kHz

(Jackson and Richardson, 2007). Hindering our understanding of backscatter mechanisms at high frequencies, and thus its interpretation, is the paucity of measurements above 100 kHz. To help elucidate the linkages between seabed properties (e.g., surface roughness) and acoustic scattering, this paper describes wideband (170–250 kHz) measurements of acoustic backscatter from sand, gravel, and bedrock seafloors collected in a coastal environment.

Few measurements of bottom scattering strength, $S_b = 10 \log 10\sigma$, have been reported at high frequencies (>100 kHz) and at large grazing angles. McKinney and Anderson (1964) provide the most extensive measurements (frequencies ranging from 12.5 to 290 kHz and grazing angles from 1° to 90°). They found that most sand substrates were associated with a mild increase S_b with increasing frequency, f ($S_b \propto 10 \log_{10} f^{1.6}$), with no frequency dependence for clayey medium sand or solid rock and large variations for solid coral. Stanic et al. (1998, Fig. 5) found that S_b increased by 10 dB between 110 and 180 kHz at a 30° grazing angle in a coarse sand environment with shell fragments present, which would equate to a frequency dependence of almost $10 \log_{10} f^5$. These measurements by Stanic et al. (1998) stand in contrast to measurements in similar environments by Stanic et al. (1989) who found a weak decrease in S_b with increasing frequency ($10 \log_{10} f^{-0.1}$) between 20 and 180 kHz at a 30° grazing angle; and to those of Williams et al. (2002, 2009) who show about a 12 dB increase in S_b between 100 and 400 kHz ($10 \log_{10} f^2$) for grazing angles of 20° and 30° (see Williams et al., 2009, Fig. 9). At a grazing angle of 15°, Greenlaw et al. (2004) found a $10 \log_{10} f^{1.4}$ frequency dependence in S_b for a sand bottom at frequencies up

[a] Electronic mail: tom.weber@unh.edu

to more than 400 kHz. Taken together, these measurements suggest that sand seafloors have a highly variable frequency dependence ranging from $10 \log_{10} f^{-0.1}$ to $10 \log_{10} f^5$, or -0.3 to 15 dB/octave, at least at somewhat small (30° or less) grazing angles.

Acoustic scattering from the seafloor is generally attributed to some combination of interface roughness and scattering from inhomogeneities within the sediment volume or at the water-sediment interface (e.g., shell debris). Sediment volume inhomogeneities may include perturbations in porosity (Hines, 1990), gas bubbles (e.g., Anderson and Hampton, 1980), bioturbation (Pouliquen and Lyons, 2002), and strong gradients in density (Lyons and Orsi, 1998). Models for oblique incidence backscatter (note that this paper will examine seabed backscatter at a 45° grazing angle) suggest that the seafloor backscatter is dependent on the roughness spectrum evaluated at the Bragg wavenumber, making the slope of the roughness spectrum an important parameter especially when examining the frequency dependence of the backscatter (Jackson and Richardson, 2007). A power-law roughness spectrum is often assumed for the seafloor. For example, sand seafloors have been found to follow a power-law spectrum following $K^{-2.5}$ to K^{-4} where K is the wavenumber (Briggs et al., 2005); a value of K^{-3} would result in a 3 dB/octave increase in seafloor backscatter following the perturbation approximation described by Jackson et al. (1986b). It seems likely that the roughness spectrum will change at the very short wavelengths, either because the dynamics governing the sediment transport process that give rise to a particular roughness do not operate at very small scales, or because a limit is reached at which the roughness becomes defined by the individual grains on the seafloor rather than by the continuum of grains at the interface. It has also been suggested that some mechanism other than the rough interface or volume scattering dominates seafloor backscatter at high frequencies, including scattering from large shell fragments (Williams et al., 2002; Lyons, 2005; Williams et al., 2009; Ivakin, 2012) and from the volume of individual grains themselves (Ivakin and Sessarego, 2007; Chotiros and Isakson, 2013).

In general, the mechanisms for scattering and the possible transition from a surface roughness mechanism to individual grains or other large scatterers are not well understood. As a step toward illuminating these mechanisms, the study presented here discusses wideband measurements of seafloor backscatter between 170 and 250 kHz and at a 45° grazing angle collected with a calibrated split-beam echosounder (SBES) mounted aboard a small survey vessel (12 m length) in December, 2013. The measurements were collected as the vessel traversed several different seafloor types, including sand seafloors with abundant and limited shell hash (loose accumulations of shell debris) and a gravel seafloor. For the purposes of this work it is assumed that the seafloor properties relevant to acoustic backscatter are locally (within 25 m) stationary, at least in areas away from sediment boundaries, in order to establish sufficiently large ensembles of measurements from which the bottom scattering strength, $S_b = 10 \log 10\sigma$, can be accurately estimated. Particular attention is paid to the frequency dependence of

S_b for the different seafloor types, and how this frequency dependence changes for the different seafloor types studies here. Complementing the acoustic data are estimates of grain size (for the sand and gravel areas) and still-images of the seafloor that provide a qualitative description of the seafloor.

II. EXPERIMENTAL SITE DESCRIPTION

Seabed backscatter was collected in lower Portsmouth Harbor, NH, a region characterized by strong tidal currents, periodic storm waves, and a heterogeneous seafloor composed of a range of sediments from muddy fine sands to pebble and cobble gravels; bedrock outcrops are also common. The seafloor in this area is typical of previously glaciated, high energy environments. Of particular interest in this work are the regions identified as the lower Portsmouth Harbor sand wave field, the mouth channel lag deposits, and the inner shelf rippled sands (Fig. 1).

These three areas were sampled using a Shipek grab sampler (Wildco, Yulee, FL) and a drop video camera. The drop video camera consisted of a Delta Vision camera (Ocean Systems, Burtonsville, MD) mounted in a frame that positioned the camera 0.4 m from the base and the seafloor (when in its vertical position). The base of the frame was 0.3×0.3 m and displayed a 2 cm interval scale. The camera has a 1.2 mm pixel resolution (Pe'eri et al., 2013). The ship's global positioning system (GPS) was recorded during both the Shipek and video deployments. Given the uncertainty of the deployed Shipek and camera positions relative to the ship's GPS, the accuracy of the sampled positions are probably no better than 10 m for the Shipek and 20 m for the video locations.

The Shipek grab sampler worked well in the sandy areas but was not able to consistently collect samples large enough for accurate analysis in pebble or cobble areas. Bottom sediments were analyzed for grain size using standard sieve and pipette analytical techniques (after Folk, 1980). The grain size data were analyzed in "Gradistat" (Blott and Pye, 2001) and the major statistics determined by the Gradistat program. The results reported here are mean grain size given in phi (ϕ) units and millimeters (mm) and a sediment name based on the Wentworth scale as discussed in Folk (1980). The full grain size distributions as a percentage of the total sample weights are provided in Table I.

The sand wave field is a major depositional feature located in Portsmouth Harbor characterized by bed forms ranging from ripples to sand waves [Figs. 1, 2(a), and 2(b)]. Grab samples collected in multiple locations (upper, middle, lower) along the sand wave field suggest that the sediment characteristics are relatively similar over the entire sediment body and are composed of primarily unimodal, very poorly sorted to moderately well sorted, slightly granular to granular medium sands with a high shell hash content. Mean grain size varied from 0.39ϕ (0.77 mm) to 1.83ϕ (0.28 mm).

The lag deposits in the channel thalweg [Figs. 1, 2(c), and 2(d)] are primarily composed of very poorly to poorly sorted sandy pebble gravels or pebble gravels, and were difficult to sample in quantities required for an accurate assessment of grain size. The samples that were collected had mean grain sizes of -1.96ϕ (3.89 mm) to -5.06ϕ
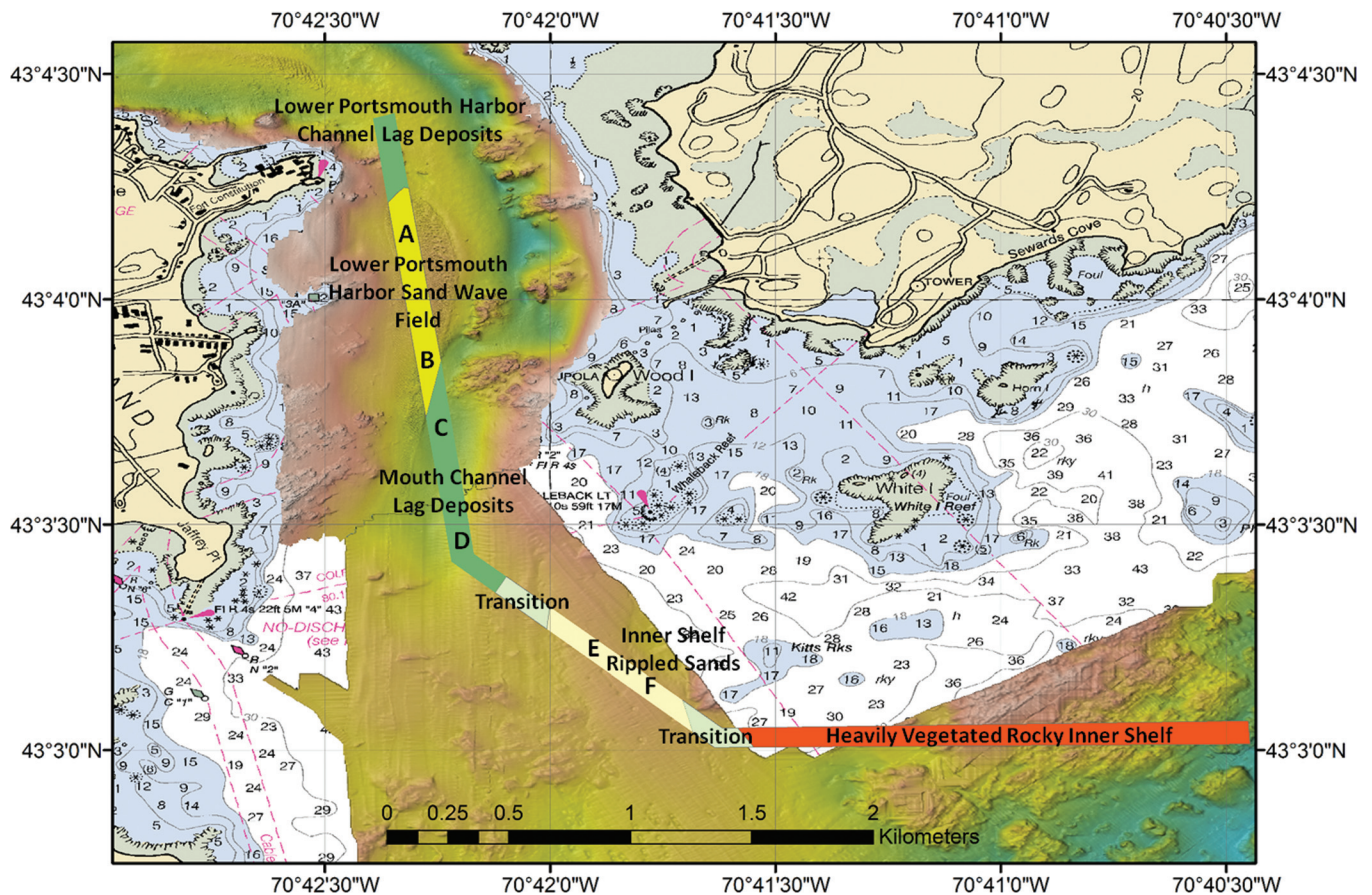
Thomas C. Weber and Larry G. Ward

FIG. 1. Experiment location and characterization of major depositional environments. Seabed sampling stations are identified by letters A–F.

(33.36 mm) with gravel contents from 61% to 97%, in qualitative agreement with the video data [Fig. 2(b)].

The inner shelf rippled sands [Figs. 1, 2(e), and 2(f)] are in an area with decreased current energy relative to the sand wave field or the channel. The sediments in this location are comprised of unimodal, poorly to well sorted, slightly granular very fine sands to pebbly very fine sands with mean grain sizes varying between 2.73ϕ (0.15 mm) and 3.02ϕ (0.12 mm), with 88%–99% sand content. Sand dollars were abundant on the western edge of this region in quantities of approximately 10–20 per square meter based on a cursory examination of the video data.

III. ACOUSTIC DATA COLLECTION AND PROCESSING

Seabed backscatter observations were collected with a single Simrad ES200-7CD SBES mounted so that its maximum response axis (MRA) was at a 45° elevation angle in the roll plane, pointing toward the port side of the vessel. The acoustic transducer was a circular "piston" transducer with a nominal 7° one-way beam width at 200 kHz. The transducer was interfaced to a prototype Simrad wideband transceiver (WBT) that contained all of the echosounder electronics: signal generator and power amplifier, receive amplification and filtering, and digitization. All parameters of the system (e.g., transmit power setting, signal type and duration, receive filter parameters) were kept constant throughout the experiment.

For the experiment described here, the transmitted signal consisted of a 2.05 ms linear-frequency-modulated signal covering a frequency range of 160–260 kHz. To minimize the transient responses of the transducer, a weighting was applied to the transmitted signal prior to signal transmission. This weighting was a Tukey window where the ratio of the taper section to the total window length is 0.2, such that the transducer was transmitting at "full-power" only between 170 and 250 kHz. In the subsequent analysis, only frequencies between 170 and 250 kHz are considered.

A. Scattering from a single discrete target: The general approach to system calibration

The SBES system was used first to observe the scattered pressure from a tungsten carbide (WC) calibration sphere (i.e., a single deterministic target) with known scattering properties in order to provide a calibration of system properties, and later used to collect observations of scattering from the seabed. Beginning with the calibration target, the scattered pressure p_s as a function of time, t, from a target at range r can be written as the convolution of a signal waveform, s_o, with the impulse response of the transmitting transducer, h_{trx}, the impulse response of the medium between the SBES and the target, h_p, and the impulse response of the target itself, h_{tg},

$$p_s(t) = s_o(t - t_o) \otimes h_{trx} \otimes h_{tl} \otimes h_{tg}. \tag{1}$$

J. Acoust. Soc. Am. **138** (4), October 2015

Thomas C. Weber and Larry G. Ward   2171

TABLE I. Size distributions for the sediment samples collected at the sampling stations shown in Fig. 1. The values for each size class are in percent (rounded to tenths) of the total sample weights unless otherwise labelled. Total sediment weight analyzed is given in bottom row of each sample. All of the samples were taken during 2013.

Size class phi (Φ)	Size class mm	July 3rd Samp 01	July 3rd Samp 02	Oct 21st Samp 01	Oct 21st Samp 02	Dec 17th Samp 01	Dec 17th Samp 02	July 3rd Samp 01	July 3rd Samp 02	Oct 21st Samp 01	Oct 21st Samp 02	Dec 17th Samp 01	Dec 17th Samp 02
		Station A	Station A	Station A	Station A	Station A	Station A	Station B	Station B	Station B	Station B	Station B	Station B
−3.0	8.00	0.0	0.0	0.0	0.0	0.4	0.0	0.9	0.0	0.0	0.0	0.0	0.0
−2.5	5.66	0.8	0.0	0.1	0.2	0.6	0.2	1.3	0.0	0.2	1.4	0.0	0.3
−2.0	4.00	0.7	0.9	1.3	1.1	0.8	0.8	1.6	1.2	0.4	2.0	1.1	0.3
−1.5	2.83	1.0	0.2	2.2	1.9	1.5	1.4	4.1	1.3	1.0	3.0	2.9	0.6
−1.0	2.00	3.2	0.7	3.5	4.3	1.8	2.4	9.6	2.6	3.4	4.9	4.5	1.2
−0.5	1.41	4.7	1.6	6.1	6.1	2.7	3.4	12.5	4.5	9.3	7.5	6.7	1.9
0.0	1.00	5.8	3.1	7.2	7.8	3.1	4.4	11.5	5.9	11.4	7.3	8.0	2.4
0.5	0.71	8.4	6.9	9.8	9.3	4.1	5.8	9.6	6.6	13.2	7.7	9.5	3.3
1.0	0.50	13.0	19.2	15.9	12.3	7.8	11.7	9.5	9.4	17.8	10.1	15.1	7.4
1.5	0.35	22.5	37.5	24.7	19.4	20.2	24.7	11.1	16.6	22.0	14.6	15.8	18.1
2.0	0.25	30.3	26.0	24.3	28.2	39.8	33.2	20.3	40.0	17.2	30.8	25.1	43.2
2.5	0.18	8.2	3.1	4.1	7.6	14.3	9.8	5.9	10.1	2.9	8.6	9.0	17.5
3.0	0.125	0.7	0.3	0.4	0.9	1.5	1.0	0.9	0.9	0.5	1.0	0.9	2.0
3.5	0.088	0.2	0.1	0.1	0.2	0.7	0.5	0.4	0.2	0.2	0.2	0.5	0.8
4.0	0.063	0.1	0.0	0.1	0.1	0.2	0.2	0.2	0.1	0.1	0.1	0.2	0.2
<4.0	<0.063	0.5	0.3	0.2	0.4	0.4	0.6	0.6	0.6	0.5	0.6	0.6	0.8
Total Sample Wt - gms		43.8	46.3	69.4	76.5	49.9	66.8	31.7	32.8	68.6	75.3	55.5	80.8
		Station C	Station C	Station C	Station C	Station C	Station C	Station D	Station D	Station D	Station D	Station D	Station D
−5.5	45.25	0.0	0.0	0.0	0.0	0.0	0.0	0.0	49.9	0.0	15.8	0.0	0.0
−5.0	32.00	0.0	0.0	45.3	17.2	0.0	0.0	22.8	9.4	0.0	0.0	0.0	0.0
−4.5	22.63	0.0	12.5	20.7	5.7	29.9	84.4	0.0	16.2	25.9	6.7	15.9	26.4
−4.0	16.00	30.8	13.1	5.1	15.0	20.8	5.4	21.6	6.6	30.6	5.7	2.9	10.0
−3.5	11.31	34.3	22.1	5.6	11.8	9.1	4.7	22.4	7.6	18.2	18.0	14.2	19.4
−3.0	8.00	4.2	9.4	2.6	4.8	3.1	0.8	8.6	5.0	6.9	17.2	15.9	8.7
−2.5	5.66	2.0	7.3	6.1	2.2	3.3	0.4	2.1	1.8	1.8	7.1	15.0	8.3
−2.0	4.00	1.3	3.7	0.6	1.6	2.3	0.3	1.1	0.8	1.0	2.9	11.3	5.2
−1.5	2.83	0.7	2.2	0.5	1.5	2.0	0.3	0.5	0.2	0.6	1.4	5.6	3.3
−1.0	2.00	1.0	1.8	0.5	1.4	1.5	0.3	0.3	0.1	0.6	1.3	2.2	1.2
−0.5	1.41	0.5	1.3	0.5	1.5	1.2	0.2	0.3	0.1	0.5	1.0	1.2	1.0
−0.0	1.00	0.4	1.2	0.4	1.3	1.0	0.2	0.4	0.1	0.3	0.7	0.7	0.6
0.5	0.71	0.5	1.3	0.4	1.4	0.9	0.1	0.5	0.1	0.3	0.7	0.5	0.5
1.0	0.50	0.7	2.0	0.6	1.9	1.5	0.1	0.8	0.1	0.4	0.9	0.7	0.7
1.5	0.35	1.9	3.6	1.7	4.3	3.4	0.3	1.4	0.1	0.6	1.5	1.4	1.3
2.0	0.25	7.7	8.6	5.1	14.0	9.9	1.1	5.5	0.4	2.9	4.8	3.8	3.8
2.5	0.18	6.1	5.2	2.5	8.7	6.2	0.7	5.0	0.4	3.7	5.6	3.2	3.5
3.0	0.125	3.5	2.3	0.9	3.2	1.8	0.3	3.8	0.5	2.9	4.3	2.6	2.7
3.5	0.088	2.2	1.2	0.3	1.3	1.1	0.2	2.0	0.3	1.9	3.2	2.0	2.3
4.0	0.063	0.6	0.4	0.1	0.3	0.2	0.1	0.5	0.1	0.3	0.4	0.3	0.3
<4.0	<0.063	1.5	1.0	0.4	0.9	0.7	0.2	0.5	0.2	0.7	0.8	0.7	0.5
Total Sample Wt - gms		129.1	318.0	509.6	429.3	515.2	342.8	556.2	448.6	384.6	727.3	456.1	496.5

TABLE I. (*Continued*)

| Size class phi (Φ)	Size class mm	July 3rd Samp 01	July 3rd Samp 02	Oct 21st Samp 01	Oct 21st Samp 02	Dec 17th Samp 01	Dec 17th Samp 02	July 3rd Samp 01	July 3rd Samp 02	Oct 21st Samp 01	Oct 21st Samp 02	Dec 17th Samp 01	Dec 17th Samp 02
		Station E	Station E	Station E	Station E	Station E	Station E	Station F	Station F	Station F	Station F	Station F	Station F
−4.0	16.00	0.0	0.0	4.0	0.0	0.0	0.0	0.0	0.0	0.0	0.0	0.0	1.8
−3.5	11.31	0.0	0.0	1.4	0.0	0.0	0.0	0.0	0.0	0.0	8.9	6.7	0.0
−3.0	8.00	0.0	0.8	1.7	0.0	0.0	0.0	0.0	0.7	0.0	0.0	3.0	0.9
−2.5	5.66	0.8	0.0	0.2	0.0	0.3	0.3	1.4	0.0	0.0	0.2	0.5	0.7
−2.0	4.00	0.0	0.1	0.1	0.1	0.2	0.0	0.5	0.1	0.9	0.5	0.3	0.4
−1.5	2.83	0.4	0.0	0.1	0.1	0.2	0.0	0.1	0.5	0.3	0.2	0.4	0.8
−1.0	2.00	0.1	0.1	0.2	0.3	0.1	0.0	0.5	0.4	0.2	0.4	0.5	0.6
−0.5	1.41	0.2	0.0	0.2	0.2	0.1	0.0	0.2	0.1	0.3	0.6	0.5	0.6
−0.0	1.00	0.4	0.1	0.1	0.2	0.1	0.0	0.4	0.4	0.4	0.6	0.5	0.6
0.5	0.71	0.5	0.2	0.2	0.3	0.1	0.1	0.7	0.6	0.5	0.6	0.6	0.6
1.0	0.50	0.8	0.4	0.3	0.5	0.2	0.2	0.9	0.9	0.5	0.7	0.6	0.7
1.5	0.35	1.9	1.1	0.7	1.0	0.6	0.5	1.5	1.4	0.9	1.1	0.9	1.0
2.0	0.25	7.0	5.4	3.3	4.5	3.1	3.1	4.6	4.1	2.8	3.1	2.7	3.0
2.5	0.18	8.1	7.9	6.4	7.8	6.6	8.0	6.0	5.7	5.1	5.5	4.8	5.2
3.0	0.125	40.7	43.4	30.7	35.2	38.0	42.9	34.9	35.8	25.1	24.6	23.7	26.3
3.5	0.088	34.9	35.8	44.0	45.8	47.2	42.3	41.0	42.2	56.5	47.9	49.2	51.6
4.0	0.063	3.2	3.5	2.0	2.7	2.4	1.9	5.5	5.8	5.0	3.9	4.2	4.2
<4.0	<0.063	1.0	1.2	4.5	1.4	0.8	0.6	1.7	1.3	1.6	1.3	0.9	1.0
Total Sample Wt - gms		45.3	50.2	95.4	52.8	69.5	56.0	36.1	41.3	58.4	64.7	54.1	61.2
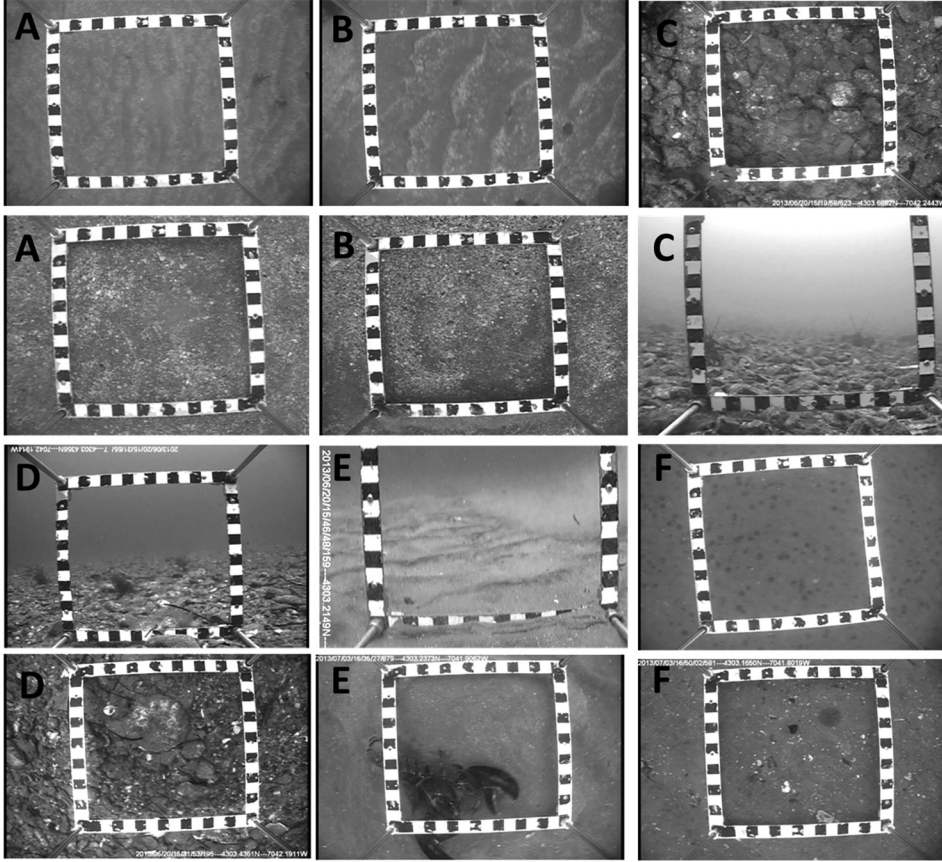
FIG. 2. Seafloor imagery for the sampling stations identified in Fig. 1 including the sand wave field [(A) and (B)], the mouth channel lag deposits [(C) and (D)], and the inner shelf rippled sands [(E) and (F)]. For each station a pair of images is shown. At stations (A), (B), and (F) the camera frame is oriented vertically and looking straight down and suspended either a few meters above the seabed (upper) or on the seabed (lower). In (C), (D), and (E) both an oblique view of the seabed and a view with the frame oriented vertically and looking down is shown; in both cases the frame is resting on the seabed. The base of the camera frame, which can be seen in each image, is comprised of 2 cm long black and white bars.

In Eq. (1), t_o represents the arrival time of the scattered wave from the target (nominally $2r/c$ where c is the speed of sound). The scattered pressure is converted into a received signal by a receiving transducer (identical to the transmitting transducer in the present case) and associated signal conditioning electronics so that the signal available for subsequent analysis can be represented as

$$s(t) = s_o(t - t_o) \otimes h_{trx} \otimes h_p \otimes h_{tg} \otimes h_{trr}. \qquad (2)$$

For the purposes of this analysis, it is assumed that the properties associated with both transmitting and receiving transducers and associated electronics, h_{trx} and h_{trr}, can be combined as $h_{tr} = h_{trx} \otimes h_{trr}$.

The Fourier transform of Eq. (2) is given by

$$S(f) = \int_{-T/2}^{T/2} s(t)e^{-j2\pi ft}dt = S_o(f)H_{tr}\frac{\exp(-2ar)}{r^2}H, \qquad (3)$$

where $S_o(f)$, H_{tr}, and H are the Fourier transforms of the signal, the combined transmit/receive transducer impulse response, and the target impulse response, respectively. T represents an analysis window which is assumed to fully encapsulate the scattered wave from the discrete target. The frequency response associated with the transmission of the signal to and back from the target is assumed to be represented by a combination of spherical spreading losses and absorption as $[\exp(-2ar)/r^2]$, where a is the absorption coefficient in units of nepers/m when the range r is in meters.

For a deterministic single target the backscattering cross section is given by

$$\sigma_{bs}(f) = |H(f)|^2. \qquad (4)$$

To calibrate the system, we make a measurement S from a target whose backscattering cross section σ_{bs} is known, convert to units that are proportional to acoustic intensity, and re-arrange Eq. (3) to isolate the system components which can be described by a single calibration factor

$$C(f) = |S_o(f)|^2|H_{tr}|^2 = \frac{|S(f)|^2}{\sigma_{bs}(f)}\frac{r^4}{\exp(-4ar)}. \qquad (5)$$

Although not required for this analysis, it is often helpful to match filter the received signal to increase the signal-to-noise ratio, to aid in the isolation of targets from reverberation, etc. The match filter applied in the present work utilizes the ideal signal, s_o, and is equivalent to multiplying the Fourier transform of the recorded signal by the complex conjugate of $S_o(f)$ so that Eq. (3) becomes

$$S_{mf}(f) = S_o(f)S_o^*(f)H_{tr}\frac{\exp(-2ar)}{r^2}H, \qquad (6)$$

and the calibration factor for the match filter output becomes

$$C_{mf}(f) = \frac{|S_{mf}(f)|^2}{\sigma_{bs}}\frac{r^4}{\exp(-4ar)}. \qquad (7)$$

B. Scattering from the seafloor

Equations (1)–(3) apply equally well when h_{tg} represents the response of the seafloor, although there are two important differences from the discrete target. The first is that the seafloor is considered to be a random process and will be examined here in terms of the statistics of an ensemble of realizations of seafloor scattering observations. The second difference is that the seafloor acts as a target that extends well beyond the observational field of view (i.e., beyond the extent of the projection of the pulse on the seabed). Unlike the single discrete target, this second difference means that magnitude of $S(f)$ will change as the length, T, of the analysis window changes.

Converting Eq. (3) into units proportional to acoustic intensity and ensemble averaging the result yields

$$\langle |S(f)|^2 \rangle = C(f) \frac{\exp(-4ar)}{r^4} \langle |H(f)|^2 \rangle, \tag{8}$$

where the brackets $\langle \rangle$ indicate an ensemble average and it is assumed that the calibration constant C and the propagation variables a and r are deterministic.

The target strength (TS) of the seafloor (in the linear domain) is given by $\langle |H(f)|^2 \rangle$, in similar fashion to that of the deterministic single target, and represents the response of the seafloor integrated over the analysis window of length T seconds. $\langle |H(f)|^2 \rangle$ can be represented by the product of the scattering cross section σ of the seafloor multiplied by the insonified area, A, such that

$$\sigma(f) = \frac{\langle |H(f)|^2 \rangle}{A} = \frac{\langle |S(f)|^2 \rangle}{C(f)} \frac{r^4}{\exp(-4ar)} \frac{1}{A}. \tag{9}$$

For the scenario used in this work where only the scattered return arriving at the transducer MRA is considered, A can be approximated as a rectangular area that is $\theta_{2eq} r$ on one side by $cT/2 \sin\theta_i$ on the other side (see Fig. 3.16 in Lurton, 2010). θ_{2eq} represents the equivalent beam width for the combined transmit and receive transducers in the direction perpendicular to the direction of propagation of the pulse projected onto the seafloor, or the along-track direction in the case of the side-looking beam examined in this work. When the same transducer is used for transmit and receive, as in the present case, θ_{2eq} is the "two-way" equivalent beam width. When projected on the seafloor the width of the equivalent beam in meters is given by the product of θ_{2eq} (in radians) and the range from the transducer to the seafloor, r. The dimension of the rectangular area A that is parallel to the direction of propagation of the pulse projected onto the seafloor (the across-track dimension in this work) is given by the length of the analysis window converted to distance using the speed of sound, c, which is then projected onto the seafloor using the angle of incidence (measured from the vertical) θ_i. Assuming knowledge of c, T, θ_{2eq}, and θ_i, σ can be calculated according to

$$\sigma(f) = \frac{\langle |S(f)|^2 \rangle}{C(f)} \frac{r^4}{\exp(-4ar)} \frac{2\sin\theta_i}{cT\theta_{2eq}r}. \tag{10}$$

If the recorded signal has been match filtered using s_o as the signal replica, Eq. (10) becomes

$$\sigma(f) = \frac{\langle |S_{mf}(f)|^2 \rangle}{C_{mf}(f)} \frac{r^4}{\exp(-4ar)} \frac{2\sin\theta_i}{cT\theta_{2eq}r}. \tag{11}$$

In this work Eqs. (7) and (11) are used to calibrate the system and estimate the scattering cross section for the seafloor, respectively.

C. Split-beam processing

Proper calibration of the SBES system requires compensation for the transducer beam pattern (the target response appears weaker off the transducer MRA than it actually is). Similarly, the use of Eq. (10) assumes that the analysis window T is restricted to a time coincident with the return from the transducer MRA in the across-track direction (i.e., perpendicular to the direction the ship is pointing). Both require estimating the target angle, which is done using the split-aperture techniques described by Burdic (1991).

The Simrad ES200-7CD transducer is divided evenly into four quadrants, and each quadrant is recorded separately. The output of the four quadrants are coherently summed to form $s(t)$, and the electrical phase difference between pairs of the quadrants (i.e., in the transducer roll and pitch planes) is used to estimate the angle. This phase difference is calculated directly from the match filter outputs, $s_{mf,i}(t) = s_i(t) \otimes s_o^*(-t)$, where the subscript i varies from 1 to 4 based on the quadrant number. Following Burdic (1991), the electrical phase angles in the transducer roll and pitch planes can be calculated as

$$\psi_1 = \tan^{-1} \frac{\text{Im}\{(s_{mf,1} + s_{mf,2})(s_{mf,3} + s_{mf,4})^*\}}{\text{Re}\{(s_{mf,1} + s_{mf,2})(s_{mf,3} + s_{mf,4})^*\}},$$

$$\psi_2 = \tan^{-1} \frac{\text{Re}\{(s_{mf,1} + s_{mf,4})(s_{mf,2} + s_{mf,3})^*\}}{\text{Re}\{(s_{mf,1} + s_{mf,4})(s_{mf,2} + s_{mf,3})^*\}}. \tag{12}$$

IV. ACOUSTIC CALIBRATION

Prior to collecting seafloor backscatter data, the SBES system was calibrated. The objectives of the acoustic calibration were to (1) understand the frequency response of the system (transducer plus transceiver electronics) in order to accurately estimate the TS of the seafloor; and (2) to estimate the frequency-dependent beam pattern of the transducer in order to estimate the area of the transducer beam footprint on the seafloor in order to convert TS to S_b. The calibration was conducted in two phases. In the first phase, the beam pattern of the transducer at 200 kHz was collected in a large, fresh-water acoustic test tank at the University of New Hampshire several weeks prior to the field data collection effort. The second phase was conducted aboard the vessel on the same day as the field experiment, and consisted of swinging a 38.1 mm WC sphere through the beam while recording data in the manner of a standard sphere calibration (Foote *et al.*, 1987).
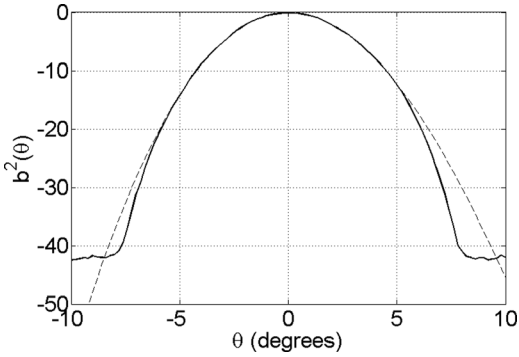
FIG. 3. Two-way beam pattern (200 kHz) of the ES200-7CD transducer measured using a 38.1 mm WC sphere in an acoustic test tank (solid line). The dashed line shows a third order polynomial fit to the beam pattern.

The 200 kHz tank calibration was conducted by controlling the orientation of the transducer in two dimensions (corresponding to the roll- and pitch-planes in the transducer reference frame) while collecting echoes from a stationary 38.1 mm WC sphere located approximately 8 m away. This calibration procedure measures the two-way beam pattern. The roll-plane two-way beam pattern, which was virtually indistinguishable from the pitch-plane two-way beam pattern, is shown in Fig. 3. The one-way equivalent beam width at 200 kHz, defined as $\theta_{1eq,200} = \int b^2 d\theta$ where it is noted that b is proportional to pressure, was calculated from these data with integral limits of $\pm 15°$ to be $\theta_{1eq,200} = 7.1°$. The two-way equivalent beam pattern (or, equivalently, the combined transmit and receive beam pattern) at 200 kHz, defined as $\theta_{2eq,200} = \int b^4 d\theta$, was calculated to be 5.0°.

The at-sea standard sphere calibration was conducted using the same transducer mount and WBT configuration that were utilized in the field data collection efforts. Data

were recorded while the sphere, which was suspended on a monofilament line attached to a hand-held pole, was swung throughout the transducer beam. To analyze the at-sea standard sphere calibration it is assumed that the transducer was axisymmetric (as suggested by the freshwater-tank results at 200 kHz). The system response, including that of the transducer and the transceiver, is examined as a function of frequency and the magnitude of the phase angle, $\psi = \sqrt{\psi_1^2 + \psi_2^2}$. At each frequency between 160 and 260 kHz, a third degree polynomial is fit to the beam pattern data for $\psi \lesssim 1.5$ radians. While a third degree polynomial is not an exact fit for the transducer beam pattern, it provides a close match above the -20 dB points in the two-way beam pattern (Fig. 3). Prior to fitting this polynomial, ψ was normalized by the frequency according to $\psi_{norm} = \psi 200/f$, where f is frequency in kHz, under the assumption that the beam width was inversely proportional to frequency.

The result of the polynomial fit is shown in Fig. 4. The result for $P(4)$ (solid line), which is the intercept of the polynomial fit at $\psi = 0$, is compared to the theoretical TS (dashed line) for a 38.1 WC sphere (Chu, 2012) in Fig. 4. The difference between these two curves provides the calibration factor $C(f)$ in dB.

The odd coefficients for the polynomial fit, $P(3)$ and $P(1)$, are essentially zero. $P(2)$, which controls the shape of the polynomial fit, shows deviations where the signal-to-noise ratio is very low (e.g., near the start/stop frequencies where the signal taper is applied, or near nulls in the sphere response). Away from these low signal-to-noise areas, between 180 and 205 kHz and 215 and 240 kHz, $P(2)$ is approximately equal to a value of -2.86. The difference between the frequency-dependent beam response as a function of phase observed during the sphere calibration and a
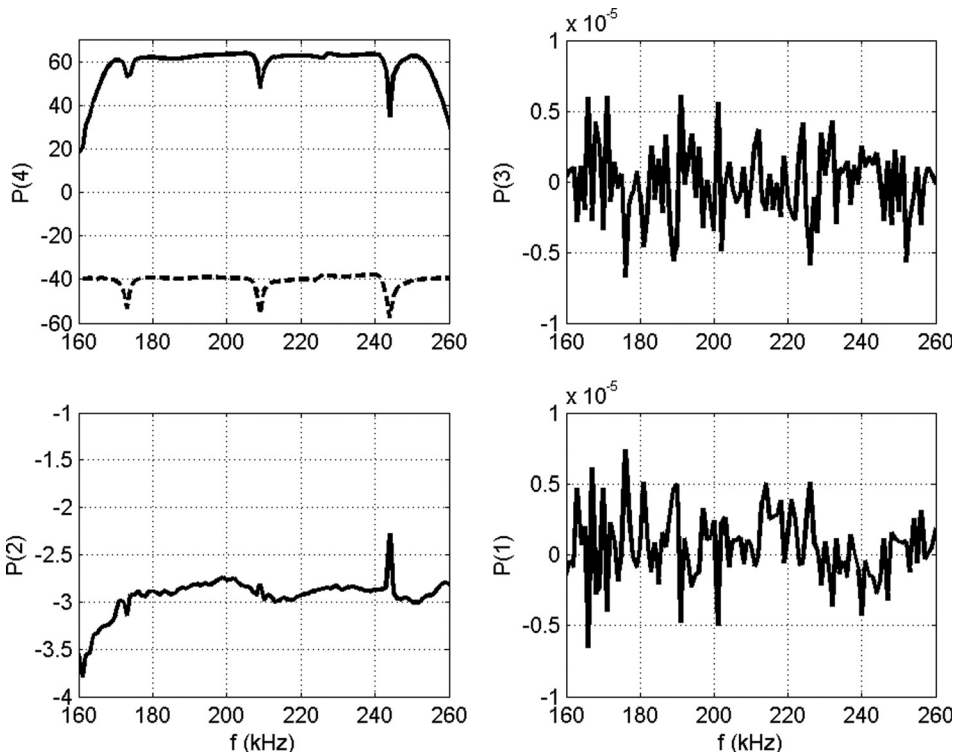

FIG. 4. Results of polynomial fit to the 38.1 mm WC sphere calibration.

Thomas C. Weber and Larry G. Ward

polynomial fit where $P(2) = -2.86$ and $P(1) = P(3) = 0$ is generally less than 0.5 dB for phase values less than 1 rad. Accordingly, it is assumed that the equivalent beam angles can be related to the 200 kHz tank observations according to

$$\theta_{1eq} = \theta_{1eq,200} \frac{200}{f},$$

$$\theta_{2eq} = \theta_{2eq,200} \frac{200}{f}. \tag{13}$$

V. OBSERVATIONS OF SEAFLOOR BACKSCATTERING STRENGTH

Immediately after conducting the at-sea field calibration, seabed backscatter observations were collected as the vessel made passage through the mouth of Portsmouth Harbor (Fig. 1) in water depths ranging from 10 to 25 m. During this time, the SBES ping rate was two pings per second. The field data were collected under calm conditions with only a few degrees of pitch and roll. Note that the vessel motion is neglected in this analysis, and consequently the results provided herein correspond to an approximately (i.e., within a few degrees) 45° grazing angle.

Raw match-filtered output ($s = 20 \log_{10}|s_{mf}(t)|$, ψ_1, and ψ_2) for a single ping are shown in Fig. 5. The match-filter output amplitude (Fig. 5, top) exhibits a typical response from the seafloor at ranges between 20 and 25 m. The roll-plane phase-angle data shows a monotonically decreasing phase angle at these ranges as the pulse travels across the beam footprint on the seafloor, similar to the split-beam phase-angle data collected by MBESs (Lurton, 2010). No trend is apparent in the pitch-angle phase-angle data due to the spread of the pulse across the beam footprint in the
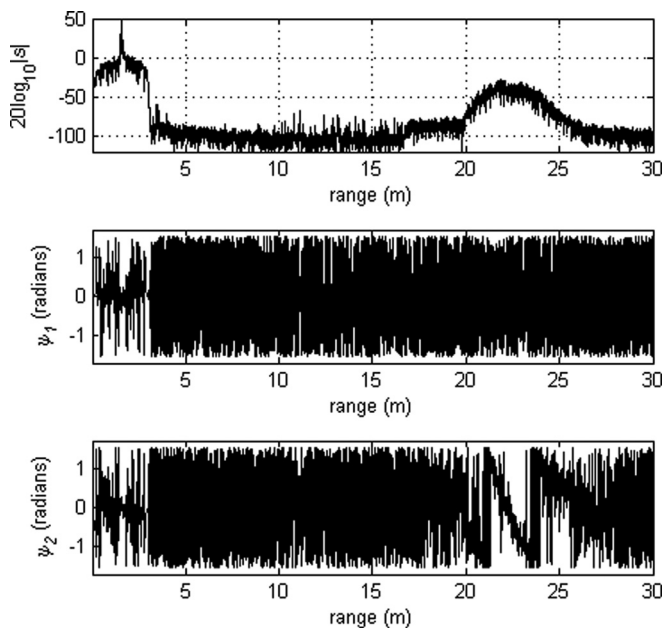

FIG. 5. An example of raw field data for a single ping including match-filtered output amplitude (top), pitch-plane phase-angle (middle), and roll-plane phase-angle (bottom). The scattered return from the seabed appears between 20 and 25 m.

along-ship direction and the resultant baseline decorrelation (Jin and Tang, 1996).

For each ping, a simple amplitude detection is performed to identify the general location of the return from the seabed, and this is used to find the location at which ψ_2 crosses zero. This zero-crossing corresponds to the range at which the seabed return is at the beam roll-plane MRA. A narrow range of data (250 samples at a sample rate of 250 ksamples/s, or approximately 0.75 m) around the zero-crossing is then used to compute $S_b(f_k) = 10 \log_{10} \sigma$ using Eq. (11) with $T = 1$ ms, θ_{2eq} given by Eq. (13) with $\theta_{2eq,200} = 5.0°$, and $\theta_i = 45°$. The frequency-dependent absorption, α, was calculated using the model of Ainslie and McColm (1998) and varied between 0.046 and 0.066 dB/m over the frequencies used here.

S_b is shown at two frequencies (170 and 250 kHz) in Fig. 6. These data have been filtered (in units proportional to intensity) using a 100-point running mean average (corresponding to 50 s of data collection and a spatial scale of approximately 150 m). These data show a high (-14 dB to -10 dB) seafloor scattering strength in the channel thalweg [ping numbers 1–200 and 750–1300; Figs. 2(C) and 2(D)], where the seafloor is comprised of sandy pebble gravels or pebble gravels, and a similarly high seafloor scattering strength over the bedrock outcrops (ping numbers 1900–2700). The sand wave field [ping numbers 250–650; Figs. 2(A) and 2(B)] exhibits a relatively lower scattering strength ranging from -21.5 to -19.5 dB. The inner shelf-rippled sands shows a more variable seabed scattering strength, starting as low as -26 dB at ping 1400 [near Fig. 2(E)], and rising to values that are higher than the sand wave field around ping 1650 [near Fig. 2(F)]. This variability and increase in seabed backscatter may be related to the sand dollars, shell fragments, and other debris that are visible in Fig. 2(F).

The difference in S_b observed at 170 and 250 kHz is small for all of the observations, and ranges from -3 to $+2$ dB (Fig. 6, bottom). Both the gravel and the bedrock seabed show a lower S_b at 250 kHz relative to 170 kHz, typically by 1–2 dB. By contrast, the sand wave field shows a higher S_b at the higher frequency by about 1 dB, reducing to
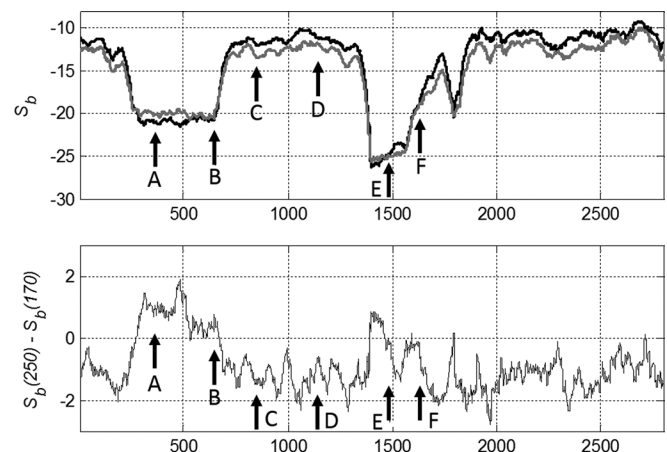

FIG. 6. S_b collected along the characterized survey line shown in Fig. 1, with the location of sampling stations noted. In the upper plot, the dark line is S_b at 170 kHz and the lighter line is S_b at 250 kHz.

J. Acoust. Soc. Am. **138** (4), October 2015

Thomas C. Weber and Larry G. Ward   2177

an indiscernible difference toward the southern edge of the sand wave field.

Observations of the full frequency-dependence in $S_b(f_k)$ are shown (Fig. 7) for the six locations described in Fig. 2. These estimates of $S_b(f_k)$ represent an average of over 100 pings. At all six locations, the frequency dependence appears weak. The data within the northern edge of the sand wave field [Figs. 2(A) and 7(A)] suggests an increase in S_b with increasing frequency that would be consistent with $S_b \propto 10 \log_{10} f^{0.32}$. The data at the southern edge of the sand wave field [Figs. 2(B) and 7(B)] appear independent of frequency. The gravelly bottoms in the channel thalweg [Figs. 2(C), 2(D), 7(C), and 7(D)] show a consistent decrease in S_b with increasing frequency similar to $S_b \propto 10 \log_{10} f^{-0.82}$ and $S_b \propto 10 \log_{10} f^{-0.67}$, respectively. The inner-shelf rippled sands [Figs. 2(E) and 2(F)] also show a consistent decrease in S_b with increasing frequency similar to $S_b \propto 10 \log_{10} f^{-0.36}$ and $S_b \propto 10 \log_{10} f^{-0.76}$ for Figs. 2(E) and 2(F), respectively.

VI. DISCUSSION

Overall trends in high-frequency backscatter for all of the regions studied, including gravel, very fine sand, medium sand, and bedrock seabeds suggest only weak frequency differences between 170 and 250 kHz (approximately half an octave). If the bottom scattering strength for the 6 locations described in Figs. 2 and 7 is controlled by the surface roughness at the Bragg scattering wavenumber, then the roughness spectrum at scales of 0.4–0.7 cm (corresponding to frequencies of 170–250 kHz and a grazing angle of 45°) would be $K^{-3.68}$ to $K^{-4.0}$ for the sand wave field, $K^{-4.67}$ to $K^{-4.82}$ for the gravel in the channel thalweg, and $K^{-4.36}$ to $K^{-4.76}$ for the inner-shelf rippled sand. These values are similar to those reported by Briggs *et al.* (2002) for similarly high spatial frequencies at a site containing medium quartz sand with 50–70 cm wavelength ripples. Briggs *et al.* (2002) found that the roughness spectrum changed slope at a spatial scale of around 0.5 cm, becoming smoother at the shorter scales ($K^{-3.8}$ to $K^{-4.39}$) and rougher at the longer scales ($K^{-1.94}$ to $K^{-3.0}$). Although this match does not provide conclusive evidence of roughness controlled scattering, it does suggest roughness scattering as a plausible mechanism for the sand wave field and the inner shelf rippled sand. On the other hand, the scales corresponding to the Bragg scattering wavenumber overlap the grain size distribution slightly (1%–2% by weight) in the largest size classes for both sand areas (Table I) and it is not possible to discount scattering by discrete inhomogeneities (e.g., shell fragments and individual grains) in the sediment volume as described by Ivakin (2012). Ivakin and Sessarago (2007) suggest a transition region based on the ratio of the mean grain size to the acoustic wavelength in water (d/λ) where the sediment properties change from that of a continuum to one where discrete grains should be considered. This ratio is approximately $d/\lambda = 0.08$ for the sand wave field and $d/\lambda = 0.02$ for the inner-shelf rippled sands, which would both be on the continuum side of the transition region of Ivakin and Sessarago (2007).

Despite the alignment between the Briggs *et al.* (2002) roughness data and the acoustic data presented here, the results for the gravel in the channel thalweg do not seem intuitive in terms of Bragg scattering. Here, the mean grain size is on the order of the acoustic wavelength or larger, suggesting that a continuum approximation for the seabed is inappropriate. Qualitatively, the gravel seafloor shown in Figs. 2(C) and 2(D) contains many angular, almost-discontinuous features that would seem to suggest
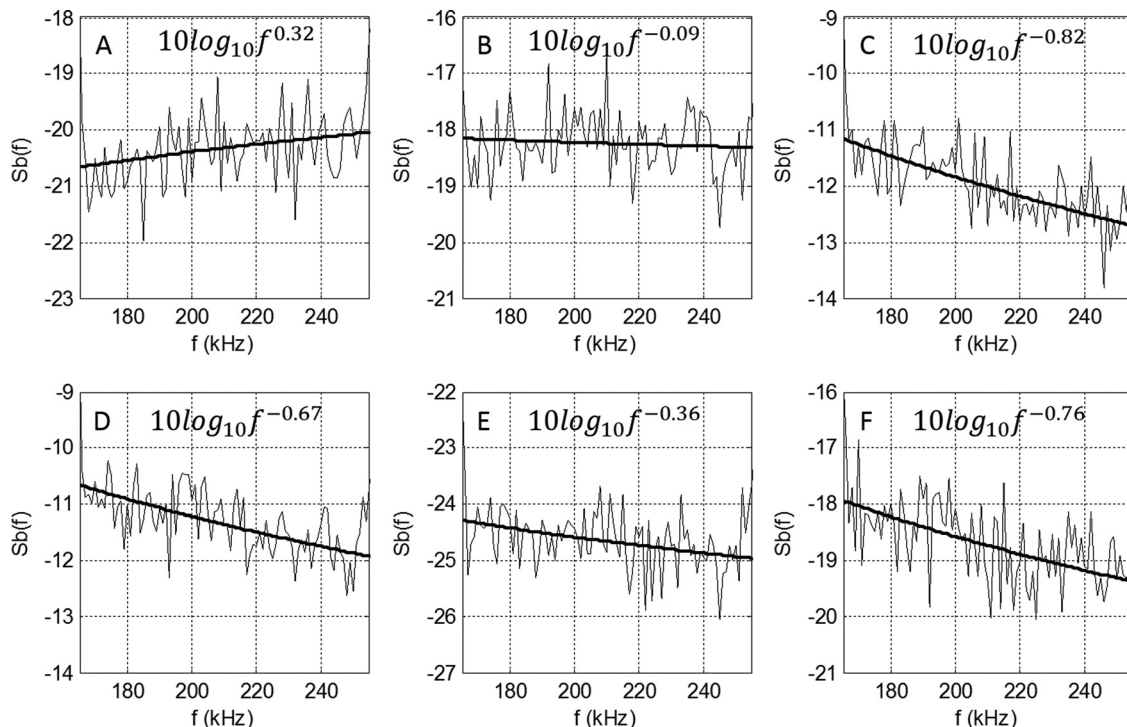

FIG. 7. Observations of $S_b(f_k)$ for the six locations described in Fig. 2. In each case, a best-fit line is heuristically calculated and overlaid on the data.

Thomas C. Weber and Larry G. Ward

substantial energy even at the high frequencies, leading to a much stronger and positive slope in the frequency dependence of S_b. For reference, Jackson *et al.* (1986a) found a somewhat weak, but positive, frequency dependence of 1.5 dB/octave for fine gravel (7.0 mm grain size, smaller than most of the gravel observed in this work) at a grazing angle of 20° and between 20 and 45 kHz (wavelengths larger than the mean grain size). It is possible that the reinforced (Bragg) scattering model is not dominating the acoustic response for the gravel seabed, and that some other mechanism is at play. At the acoustic scales relevant here, and given both the high acoustic impedance mismatch between the gravel and the seawater as well as microtopography of the seafloor which seems dominated by scales of a few cm and less, it is possible that multiple scattering at the interface (with presumably negligible penetration into the bed) is playing an important role and that the multiple scattered paths are increasingly canceling each other as the acoustic scales decrease. If this were the case, then it might be expected to see a very sharp transition in the frequency response between the lower frequencies (where the multiply scattered paths would coherently combine) and the higher frequencies where deconstructive interference would be more prevalent. A lower frequency measurement would be required to determine if this scenario were true.

It is interesting to note that the observed S_b is quite strong for the channel lag deposits and the rocky inner shelf strong (Fig. 6). While these measurements are only at one angle and cannot be used to assess whether the data satisfy the requirement for conservation of energy, the observed backscattering cross sections sometimes approach (but do not exceed) the maximal Lambert case (Jackson and Richardson, 2007). This suggests that S_b should have a weak angular dependence at these locations in comparison to the sand wave field. It also suggests that the rate of increase in S_b with decreasing frequency [Figs. 7(C) and 7(D)] cannot extend too low in frequency, and it is speculated that a maximal S_b exists at a frequency (lower than those observed here) that may be associated with some characteristic length scale where diffuse scattering reaches a maximum for these seabeds.

While the data presented here do not conclusively identify the dominant scattering mechanisms for high-frequency scattering in sand and gravel seabeds, they are suggestive of Bragg scattering is a plausible mechanism for the sand wave fields. The mechanisms explaining the scattering from the gravel seabed are less obvious, although it would appear that the simple Bragg scattering concepts are not a satisfactory explanation. To further elucidate these mechanisms, both a wider range of acoustic frequencies and quantitative estimates of the roughness spectrums in these environments are desirable.

ACKNOWLEDGMENTS

Ainslie, M. A., and McColm, J. G. (**1998**). "A simplified formula for viscous and chemical absorption in sea water," J. Acoust. Soc. Am. **103**(3), 1671–1672.

Anderson, A. L., and Hampton, L. D. (**1980**). "Acoustics of gas-bearing sediments I. Background," J. Acoust. Soc. Am. **67**(6), 1865–1889.

Blott, S. J., and Pye, K. (**2001**). "Gradistat: A grain size distribution and statistics package for the analysis of unconsolidated sediments," Earth Surf. Processes Landforms **26**, 1237–1248 (2001).

Briggs, K., Lyons, A., Pouliquen, E., Mayer, L., and Richardson, M. (**2005**). "Seafloor roughness, sediment grain size, and temporal stability," in *Proceedings of the International Conference on Underwater Acoustic Measurements: Technologies and Results*, edited by J. P. Papadakis and L. Bjorno, Heraklion, Crete, pp. 337–343.

Briggs, K. B., Tang, D., and Williams, K. L. (**2002**). "Characterization of interface roughness of rippled sand off Fort Walton Beach, Florida," IEEE J. Ocean. Eng. **27**(3), 505–514.

Burdic, W. S. (**1991**). *Underwater Acoustic System Analysis*, 2nd ed. (Prentice Hall, Englewood Cliffs, NJ), pp. 328–331.

Chotiros, N., and Isakson, M. (**2013**). "High frequency backscattering from sandy sediments: Single or multiple scattering," Proc. Meet. Acoust. **19**(1), 070011.

Chu, D. (**2012**). (private communication).

Folk, R. L. (**1980**). *Petrology of Sedimentary Rocks* (Hemphill Publishing Co., Austin, TX), 182 pp.

Fonseca, L., and Mayer, L. (**2007**). "Remote estimation of surficial seafloor properties through the application angular range analysis to multibeam sonar data," Mar. Geophys. Res. **28**(2), 119–126.

Foote, K., Knudsen, H., Vestnes, G., MacLennan, D., and Simmonds, E. (**1987**). "Calibration of acoustic instruments for fish density estimation," ICES Coop. Res. Report, Vol. 144, 81 pp.

Greenlaw, C. F., Holliday, D. V., and McGehee, D. E. (**2004**). "High-frequency scattering from saturated sand sediments," J. Acoust. Soc. Am. **115**(6), 2818–2823.

Hines, P. C. (**1990**). "Theoretical model of acoustic backscatter from a smooth seabed," J. Acoust. Soc. Am. **88**(1), 324–334.

Ivakin, A., and Sessarego, J. (**2007**). "High frequency broad band scattering from water-saturated granular sediments: Scaling effects," J. Acoust. Soc. Am. **122**(5), EL165–EL171.

Ivakin, A. N. (**2012**). "Sound scattering by the seafloor: Results of recent theoretical and experimental research," Acoust. Phys. **58**(2), 187–191.

Jackson, D. R., Baird, A. M., Crisp, J. J., and Thomson, P. A. (**1986a**). "High-frequency bottom backscatter measurements in shallow water," J. Acoust. Soc. Am. **80**(4), 1188–1199.

Jackson, D. R., and Richardson, M. (**2007**). *High-frequency Seafloor Acoustics* (Springer, New York), pp. 24–26, 338, 348–353.

Jackson, D. R., Winebrenner, D. P., and Ishimaru, A. (**1986b**). "Application of the composite roughness model to high-frequency bottom backscattering," J. Acoust. Soc. Am. **79**(5), 1410–1422.

Jin, G., and Tang, D. (**1996**). "Uncertainties of differential phase estimation associated with interferometric sonars," IEEE J. Ocean. Eng. **21**(1), 53–63.

Lurton, X. (**2010**). *Introduction to Underwater Acoustics* (Springer, New York), pp. 102 and 351–369.

Lyons, A. P. (**2005**). "The potential impact of shell fragment distributions on high-frequency seafloor backscatter," IEEE J. Ocean. Eng. **30**(4), 843–851.

Lyons, A. P., and Orsi, T. H. (**1998**). "The effect of a layer of varying density on high-frequency reflection, forward loss, and backscatter [seafloor acoustics]," IEEE J. Ocean. Eng. **23**(4), 411–422.

McKinney, C. M., and Anderson, C. D. (**1964**). "Measurements of backscattering of sound from the ocean bottom," J. Acoust. Soc. Am. **36**(1), 158–163.

Pe'eri, S., McLeod, A., Lavoie, P., Ackerman, S., Gardner, J., and Parrish, C. (**2013**). "Field calibration and validation of remote-sensing surveys," Int. J. Remote Sens. **34**(18), 6423–6436.

Pouliquen, E., and Lyons, A. P. (**2002**). "Backscattering from bioturbated sediments at very high frequency," IEEE J. Ocean. Eng. **27**(3), 388–402.

Rzhanov, Y., Fonseca, L., and Mayer, L. (**2012**). "Construction of seafloor thematic maps from multibeam acoustic backscatter angular response data," Comp. Geosci. **41**, 181–187.

Stanic, S., Briggs, K. B., Fleischer, P., Sawyer, W. B., and Ray, R. I. (**1989**). "High-frequency acoustic backscattering from a coarse shell ocean bottom," J. Acoust. Soc. Am. **85**(1), 125–136.

Stanic, S., Goodman, R. R., Briggs, K. B., Chotiros, N. P., and Kennedy, E. T. (**1998**). "Shallow-water bottom reverberation measurements," IEEE J. Ocean. Eng. **23**(3), 203–210.

Williams, K. L., Jackson, D. R., Tang, D., Briggs, K. B., and Thorsos, E. I. (**2009**). "Acoustic backscattering from a sand and a sand/mud environment: Experiments and data/model comparisons," IEEE J. Ocean. Eng. **34**(4), 388–398.

Williams, K. L., Jackson, D. R., Thorsos, E. I., Tang, D., and Briggs, K. B. (**2002**). "Acoustic backscattering experiments in a well characterized sand sediment: Data/model comparisons using sediment fluid and Biot models," IEEE J. Ocean. Eng. **27**(3), 376–387.